ACS Catalysis

pubs.acs.org/acscatalysis Research Article

One-Step Chemical Vapor Deposition Synthesis of Hierarchical Ni and N Co-Doped Carbon Nanosheet/Nanotube Hybrids for Efficient Electrochemical CO_2 Reduction at Commercially Viable Current Densities

Yang Gang, Erik Sarnello, John Pellessier, Siyuan Fang, Manuel Suarez, Fuping Pan, Zichen Du, Peng Zhang, Lingzhe Fang, Yuzi Liu, Tao Li, Hong-Cai Zhou, Yun Hang Hu, and Ying Li*

Cite This: *ACS Catal.* 2021, 11, 10333−10344 Read Online

ACCESS | Metrics & More | Article Recommendations | Supporting Information

ABSTRACT: Carbon catalysts with metal and nitrogen dopants hold significant promises for an electrochemical CO_2 reduction reaction (CO_2RR). However, the fabrication of these carbon catalysts normally requires an energy-intensive synthesis process. Traditionally, 2D graphene and 1D carbon nanotubes (CNTs) are the most widely used carbon supports, but graphene tends to aggregate and CNTs suffer from low density of active sites on the surface. In this work, we developed a 3D hybrid carbon nanosheet/nanotube catalyst with nickel (Ni) and nitrogen (N) co-doped active sites for the CO_2RR by a one-step chemical vapor deposition (CVD) method. Both single atomic sites and nanoparticles of Ni were observed on the hybrids, but the Ni nanoparticles were encapsulated by graphitic carbon layers during the CVD process, and as a result, the competing hydrogen evolution reaction was suppressed and high CO selectivity was achieved. The as-prepared catalyst with 20 min CVD delivered a stable CO Faradaic efficiency of 91% with a partial current density of 28.9 mA/cm^2 at −0.74 V in an H-cell setup. The same catalyst achieved a commercially viable current density of 600 mA/cm^2 in a flow cell with CO selectivity above 85%, at an applied voltage of −2.0 V vs reversible hydrogen electrode without iR compensation. To the best of our knowledge, these results are among the best performances in the literature in terms of both current density and CO selectivity for the CO_2RR by carbon-based catalysts. Furthermore, catalysts developed in this work are synthesized at a moderate temperature without any acid/oxidant pretreatment or post-washing. The energy-efficient and environmentally benign synthesis and the significantly high performance of catalysts are essential to future large-scale CO_2RR applications.

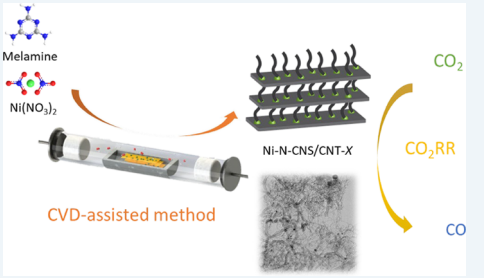

KEYWORDS: *CO_2 reduction, chemical vapor deposition, environmentally benign manufacturing, carbon nanotube/nanosheet hybrid, commercially viable current density*

1. INTRODUCTION

To mitigate the global warming effect, technologies have been developed to reduce CO_2 emissions, capture CO_2 from the emission source or directly from the atmosphere, or convert it back into useful fuels and chemicals through catalytic approaches.[1−5] Among them, an electrochemical CO_2 reduction reaction (CO_2RR) to generate value-added products powered by renewable energy sources such as solar and wind provides a sustainable solution. Carbon-based catalysts doped with earth-abundant transition metals (Fe, Ni, Co, etc.) and nitrogen (N) species (M-N-C) are an emerging type of catalysts and are demonstrated as a promising cost-effective alternative to noble metal catalysts.[6−10] The nitrogen-coordinated metal active sites (M-N) could activate CO_2 to a COOH* intermediate,[11−13] making the M-N-C catalyst one of the best for reducing CO_2 to CO in a neutral aqueous environment.[6,7,11,13]

The structure of carbon supports of the M-N-C catalyst plays a significant role in the performance of the CO_2RR as the structure affects the mass transport of reactants in the local gas-catalyst-electrolyte triphasic interface.[14] Layer-structured materials such as graphene[13,15] and one-dimensional (1D) materials such as CNTs[16,17] are the most widely used carbon supports of CO_2RR catalysts. Layer-structured catalysts can provide a decent amount of doped metal/nitrogen elements with a uniform dispersion of M-N sites on or between the two-dimensional (2D) basal planes. However, 2D layers are easily

Received: April 23, 2021
Revised: July 24, 2021

https://doi.org/10.1021/acscatal.1c01864
ACS Catal. 2021, 11, 10333−10344

aggravated during preparation, storage, and reaction due to the strong π-π interaction between layers,[18] significantly reducing the electrocatalytic performance and stability with overall porosity decreasing. On the other hand, 1D CNT-based catalysts suffer from the low density of M-N active sites since the traditional oxidation/doping methods only anchor active sites on the outermost surface, and conventional methods based on CNTs are difficult to synthesize a hierarchical network.[19−21] As a result, three-dimensional (3D) hierarchical structures that integrate the advantages of both 1D and 2D structures with promoted mass transport and high electronic conductivity have attracted much attention in the CO_2RR research community.[22−25]

The state-of-the-art methods for preparing M-N-C catalysts include chemical vapor deposition (CVD) with a gas-phase carbon precursor (CH_4, C_2H_2, etc.),[31] carbon treated with nitrogen plasma[30] or pyrolysis under an ammonia atmosphere, and thermal annealing of different types of carbon using silica as hard templates,[26,27] metal organic frameworks (MOF) as soft templates, sacrificial polymers as precurosrs,[10,28] etc. Among these synthesis methods, CVD has been used to synthesize 3D metal and nitrogen-doped graphene/CNT hybrids because of its highly tunable nature compared to traditional thermal pyrolysis, making it preferable for constructing specific structures. However, there are a few drawbacks or challenges in conventional CVD methods for 3D carbon synthesis: (1) multistep CVD syntheses are typically used to generate CNTs and graphene;[29−32] (2) high energy input is always involved due to the high-temperature condition (usually 1000 °C) required to synthesize graphene by CVD;[31,33] (3) an additional step of acid washing is usually required to remove bulk metal catalysts from the substrate after CVD; (4) N-doping is typically achieved by gaseous nitrogen precursors, e.g., ammonia (NH_3) or acetonitrile (CH_3CN), and the N doping level is lower (less than 3%) compared to traditional solid nitrogen sources.[33−35] As a result, few reports in the literature have demonstrated high-performing 3D carbon structures for the CO_2RR synthesized by a CVD method. Therefore, there is still a high demand for a facile and low-cost method to synthesize 3D M-N-C catalysts for efficient CO_2RR application.

A modified, one-step CVD synthesis method developed in this work grows CNTs on a pre-prepared solid substrate, i.e., a carbon- and nitrogen-containing nanosheet structure with deposited metal seeds, so that the overall procedure of synthesizing the ultimate 3D M-N-C catalyst is simpler and can be accomplished at a lower temperature (650 °C). In brief, nickel nitrate and melamine were mixed and polymerized to synthesize polymerized carbon nitride (pC_3N_4) as the backbone with a uniform Ni distribution.[36,37] The as-prepared sample then went through a CVD process, during which CNS were generated from pC_3N_4 decomposition and CNTs were grown from the planted Ni seeds on the CNS using acetylene (C_2H_2) as the carbon precursor. The thermally instable nature of pC_3N_4 at high temperatures (>700 °C) matches the temperature of CNT growth (>650 °C), making the one-step synthesis possible. The grown CNTs would link the CNS layers, forming a unique 3D hierarchical structure. From the literature, it is possible that the CVD process could also dope nitrogen on the CNT surface, which provides the extra nitrogen seeds besides pC_3N_4 for further creating Ni-N sites.[38−40] It is hypothesized that both Ni nanoparticles (NPs) and atomic Ni sites could exist on the hybrid material, but the grown CNTs might encapsulate the Ni nanoparticles so that only the single atomic sites are exposed,[41−46] making it a highly selective CO production catalyst, suppressing the hydrogen evaluation reaction (HER) that is more favorable on the sites of Ni nanoparticles.[47,48] Thus, the post-synthesis acid washing was eliminated. The catalysts prepared by different periods of CVD growth and the resulting hybrid CNS/CNT structures were characterized and correlated with their CO_2RR activities and product selectivity.

2. EXPERIMENTAL SECTION

2.1. Synthesis of Catalysts. A typical catalyst synthesis process is shown in Figure 1. First, 2 g of melamine (Acros Organics, >99%) was mixed with 15 mL of DI water and sonicated for 15 min; meanwhile, 6 mg of $Ni(NO_3)_2{\cdot}6H_2O$ (Sigma-Aldrich, crystalline) was dissolved in 5 mL of DI water and dripped into the melamine mixture drop by drop. The mixture was further sonicated for 5 min and then transferred to a stirring hot plate at 300 rpm and 50 °C uncovered, until the water fully evaporated. The remaining powder was ground to homogeneity, placed in a crucible, and pyrolyzed in air at 550 °C for 2 h at a heating rate of 10 °C/min. The resulting powder (denoted as NiO-pC_3N_4) was transferred to an alumina boat for further CVD process.

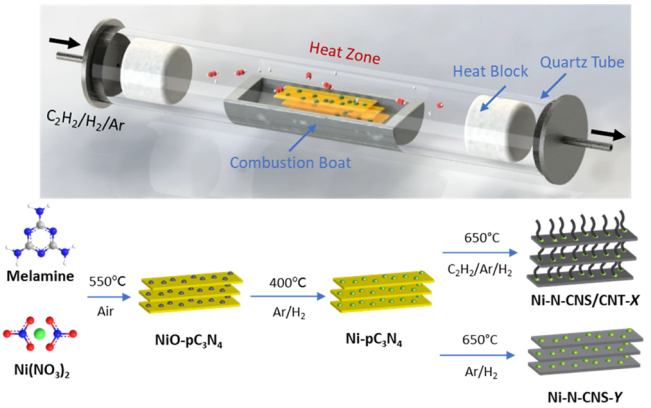

Figure 1. Schematic illustration of the experimental setup and process of the catalyst synthesis.

The CVD process was carried out in a tube furnace under 250 sccm (standard cubic centimeter per minute) Ar (Airgas, UHP grade) and 50 sccm H_2 (UHP grade). The temperature was first increased to 400 °C at a heating rate of 10 °C/min and held constant at 400 °C for 30 min to reduce NiO-pC_3N_4 into Ni-pC_3N_4. The temperature was further increased to 650 °C at a heating rate of 5 °C/min under 250 sccm of Ar and 50 sccm of H_2. With the flow rate of Ar and H_2 kept constant, another 25 sccm of C_2H_2 (dissolved grade, Western International Gas & Cylinders, Inc.) was introduced once the temperature reached 650 °C, the condition of which was then maintained for X min (X = 5, 20, or 60) before the heat source and C_2H_2 feed were shut down. The system was then cooled down naturally under 250 sccm of Ar and 50 sccm of H_2. The obtained catalyst was denoted as Ni-N-CNS/CNT-X. Two control groups were synthesized when no C_2H_2 was introduced after the temperature reached and maintained at 650 °C for Y min, i.e., Ni-N-CNS-Y (Y = 0 or 20).

For comparison, Ni-N-CNS/CNT-20 was dispersed in the 3 M HCl solution and stirred for 24 h. The sample was then

https://doi.org/10.1021/acscatal.1c01864
ACS Catal. 2021, 11, 10333−10344

centrifuged, washed with water and ethanol, and placed in a 60 °C oven overnight. The as-prepared powder is denoted as Ni-N-CNS/CNT-20-acid.

2.2. Materials Characterizations. Morphology, structure, and composition of the catalysts were characterized by scanning electron microscopy (SEM, JEOL JSM7500F), transmission electron microscopy (TEM, FEI Tecnai G2 F20 ST), high-angle angular dark-field scanning transmission electron microscopy (Hitachi 2700C), X-ray diffraction (XRD, BRIKER D8), Raman spectroscopy (Horiba Jobin Yvon LabRam HR), X-ray photoelectron spectroscopy (XPS, Omicron), and Brunauer−Emmett−Teller (BET) surface area analysis (Micromeritics ASAP 2420 physisorption analyzer). The X-ray absorption spectroscopy (XAS) measurements were performed at the 20-BM beamline of the Advanced Photon Source (APS) at the Argonne National Laboratory (ANL).

2.3. Electrochemical CO_2RR Activity Measurements. To demonstrate the CO_2RR performance of Ni-N-CNS/CNT-20 and compare it with the literature reports, two different types of cells were used in this work, as shown in Figure S1. A traditional H-cell system (Figure S1a) was used to conduct electrochemical characterizations and study the fundamentals in catalytic performance−structure relations. A flow cell setup (Figure S1b) was used to demonstrate the potential of the catalyst for industrial applications when operating at commercially viable current densities.[49]

2.3.1. H-Cell. The electrochemical CO_2RR activity measurements were conducted in a two-compartment, three-electrode H-cell system, where CO_2-saturated 0.5 M $KHCO_3$ was the electrolyte (pH 7.2), a Pt mesh (1 cm^2) was the counter electrode, and Ag/AgCl (3 M KCl) was the reference electrode, as depicted in Figure S1a. The measured potentials after iR compensation were rescaled to the reversible hydrogen electrode by E (RHE) = E (Ag/AgCl) + 0.210 V + 0.0591 V × pH. The working electrode was prepared by drop casting the catalyst ink onto a Toray carbon paper with the catalytic geometric area being 1.0 cm^2 and the catalyst mass loading being 1.0 mg/cm^2. The ink was prepared by dispersing 3 mg of catalysts into a mixture of 370 μL of ethanol, 200 μL of DI water, and 30 μL of 5% Nafion solution under sonication for 3 h. The working and reference electrodes were placed in the cathode chamber and the counter electrode in the anode chamber. The two compartments were separated by a Nafion 115 proton exchange membrane (Beantown Chemical, 0.125 mm thick) to avoid reoxidation of CO_2RR-generated products. High purity CO_2 (99.999%, Airgas) at a flow rate of 34 sccm was first introduced into the cathode chamber for 1 h to fully saturate the electrolyte before the electrolysis, and the flow rate was maintained during the electrolysis. The gas-phase products were analyzed via an online gas chromatograph (GC, Fuel Cell GC-2014ATF, Shimadzu) equipped with a thermal conductivity detector (TCD) and a methanizer-assisted flame ionization detector (FID). Any potential liquid products in the electrolyte after the reaction were analyzed by ^{1}H nuclear magnetic resonance (NMR). Typically, 450 μL of catholyte was collected after 2 h of CO_2 reduction at −0.66 V versus RHE, and 10 mg of 1,3,5-trioxane was added to the catholyte as the internal standard. The liquid sample was then transferred to 450 mL of deuterated dimethyl sulfoxide (DMSO) and subjected to analysis.

2.3.2. Flow Cell. As shown in Figure S1b, the flow cell measurement was conducted in a customized flow cell that has two compartments separated by an anion exchange membrane (Fumasep PK 130, Fuel Cell Stores). Ni foam was used as the anode (active area: 1 cm^2) and 1 M KOH anolyte was circulating in the anode chamber (flow rate: 10 mL/min) and carrying out the generated O_2 on the anode. The catholyte was also 1 M KOH, which was circulating in the cathode chamber at a flow rate of 1.5 mL/min. The cathode (active area: 1 cm^2) was prepared by airbrushing the catalyst ink (10 mg of catalyst, 3 mL of ethanol, and 0.3 mL of 5% Nafion solution) directly onto the gas diffusion layer (GDL) (Sigracet 39 BC, Fuel Cell Store). The catalyst loading is 0.8 mg/cm^2 based on the electrode weight gain after the spraying. CO_2 gas was circulated on the back side of the GDL, diffused into the GDL, and reacted at the interface of the catalyst and catholyte. A Hg/HgO electrode (1 M KOH) was used as the reference. The flow cell tests were powered by a DC power supply (Agilent E3633A), and the potential between the reference electrode and cathode was measured by a multimeter (AidoTek VC97+).[19,50,51] All the measured potentials were reported without iR compensation. The gas-phase products in the flow cell systems were analyzed via an online gas chromatograph (GC, GC-2010, Shimadzu) equipped with a thermal conductivity detector (TCD) and flame ionization detector (FID). Both CO and H_2 were detected by the TCD, and methane and hydrocarbons were measured by the FID detector.

3. RESULTS AND DISCUSSION

3.1. Morphology, Structure, and Composition. Morphology and structure of samples with different CVD process times from 0 to 60 min were characterized by scanning electron microscopy (SEM). The Ni-N-CNS-0 sample (Figure 2a) shows a flake structure (CNS) without obvious

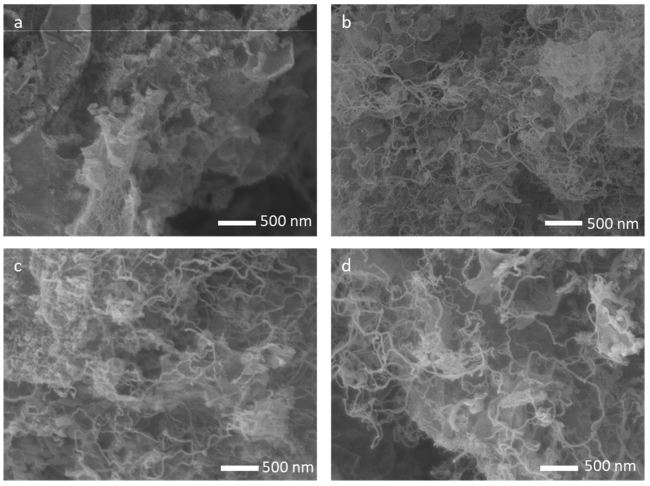

Figure 2. SEM images of (a) Ni-N-CNS-0, (b) Ni-N-CNS/CNT-5, (c) Ni-N-CNS/CNT-20, and (d) Ni-N-CNS/CNT-60.

observation of CNTs due to the absence of CVD. With 5 min CVD, CNTs started to deposit upon the introduction of C_2H_2, as observed in the Ni-N-CNS/CNT-5 sample (Figure 2b), where CNTs were densely distributed on the CNS surface. The two samples Ni-N-CNS/CNT-20 (Figure 2c) and Ni-N-CNS/CNT-60 (Figure 2d) were formed with a longer CVD time, 20 and 60 min, respectively; however, they possess a similar hybrid structure to that of Ni-N-CNS/CNT-5. As a comparison, the control group Ni-N-CNS-20 (Figure S2), which was subject to 650 °C for 20 min without C_2H_2

https://doi.org/10.1021/acscatal.1c01864
ACS Catal. 2021, 11, 10333−10344

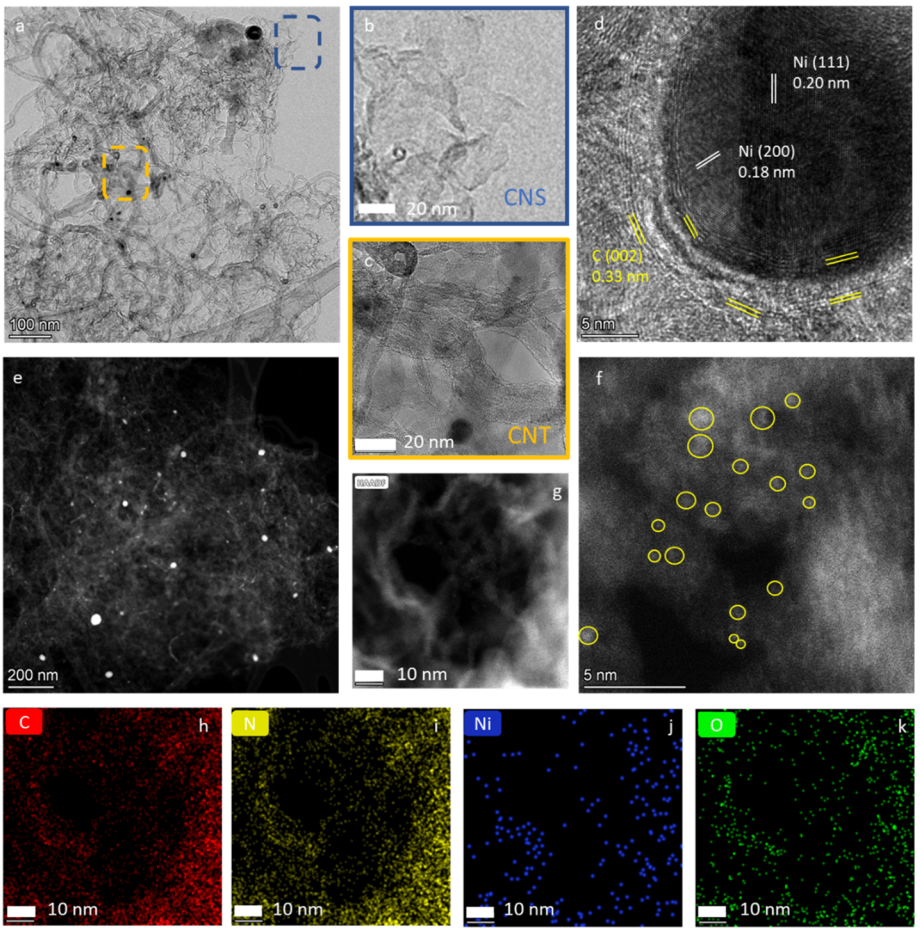

Figure 3. (a–c) TEM image, (d) HR-TEM Ni nanoparticle image, (e, f) HAADF-STEM images, and (g–k) EDS elemental mapping images of Ni-N-CNS/CNT-20.

introduction, shows mostly a flake structure similar to Ni-N-CNS-0, confirming the importance of C_2H_2 to the growth of CNTs. The different structures between Ni-N-CNS/CNT-20 and Ni-N-CNS-20 suggest that CNTs were mainly grown from the decomposed C_2H_2 during the CVD process rather than from the decomposed pC_3N_4.

Transmission electron microscopy (TEM) and high-angle angular dark-field scanning transmission electron microscopy (HAADF-STEM) were performed to further reveal the support structure and Ni dispersion level. From the TEM images, Ni nanoparticles are observed in all the samples. Ni-N-CNS-0 (Figure S3a) and Ni-N-CNS-20 (Figure S3d) revealed mostly flake structures without obvious CNT observation. Ni-N-CNS/CNT-5 (Figure S3b), Ni-N-CNS/CNT-20 (Figure 3a), and Ni-N-CNS/CNT-60 (Figure S3c) revealed clear CNS and CNT hybrid structures, which are shown in larger magnification in Figure 3b,c, respectively, in line with the SEM observation. The tube diameter ranges around 5–20 nm. High-resolution TEM (HR-TEM) was further carried out to reveal the structure and the crystal phase of carbon and nickel. The lattice spacings of the Ni nanoparticle (Figure 3d) are measured to be 0.20 and 0.18 nm along two directions, close to the *d* value of Ni (111) and Ni (200) planes, respectively.[52] Carbon layers are found wrapping the Ni particles, with a lattice spacing of 0.33 nm, corresponding to the *d* value of the C (002) plane. The thickness of the observed multilayer carbon is around 5 nm, which is consistent in different Ni nanoparticles (Figure S4). The structure of Ni-N-CNS/CNT-20 (Figure 3e) was further revealed by HAADF-STEM, showing a similar morphology to that observed in the TEM image. As shown in Figure 3f, individual bright dots can be directly observed, indicating the existence of Ni atomic sites. Energy-dispersive X-ray spectroscopy (EDS) images (Figure 3g–k) further confirm the uniform dispersion of Ni, N, and O elements on the carbon support.

The crystallinity of carbon and nickel were investigated by X-ray diffraction (XRD), as shown in Figure 4a. The NiO-pC_3N_4 showed typical pC_3N_4 patterns with a sharp C (002) peak,[53] and Ni related peaks were absent possibly due to the low concentration of Ni elements in NiO-pC_3N_4. Ni-N-CNS-0 and Ni-N-CNS/CNT-*X* showed mixed patterns including Ni (111), Ni (200), Ni (220), and broad C (002) peaks corresponding to polycrystalline carbon, in line with TEM and STEM observations. The XRD results confirm the material transformation during the CVD process from pC_3N_4 to polycrystalline carbon, which is the typical carbon structure in nitrogen-doped carbon catalysts.[10,22,54]

Nitrogen adsorption and desorption analyses were carried out to further reveal the Brunauer–Emmett–Teller (BET) surface area of each sample. As revealed by the BET isotherms in Figure S5a, NiO-pC_3N_4 showed a low adsorption quantity with a BET surface area of 7.6 m^2/g (Table S1), indicating a bulk structure with few pores. Ni-N-CNS-*Y* (Figure S5b) has a much larger absorption quantity with strong absorption in the low relative pressure range (P/P_0 = 0–0.1) and a distinct hysteresis loop in the larger pressure range (P/P_0 > 0.5),

https://doi.org/10.1021/acscatal.1c01864
ACS Catal. 2021, 11, 10333–10344

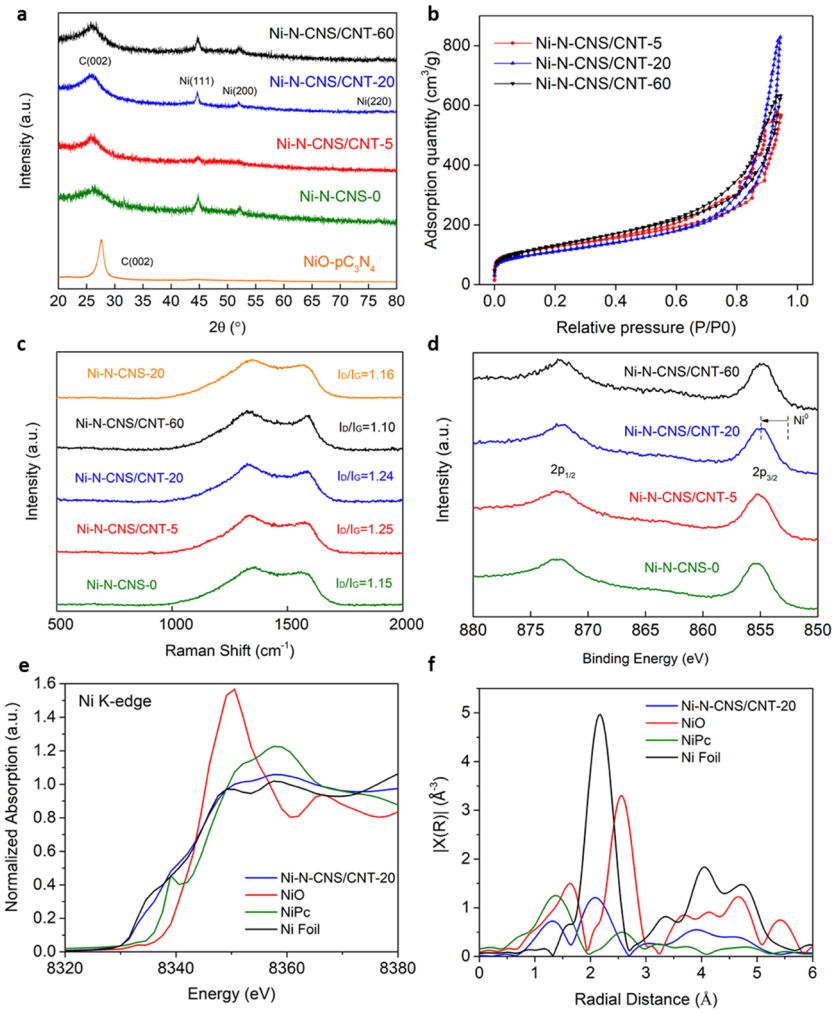

Figure 4. (a) XRD patterns, (b) BET isothermal plots, (c) Raman spectra, and (d) XPS Ni $2p_{3/2}$ spectra of Ni-N-CNS/CNT-*X*. (e) XANES and (f) EXAFS spectra for Ni-N-CNS/CNT-20 and standard references.

corresponding to the micropores and mesopores, respectively.[55] The BET specific surface areas of Ni-N-CNS-0 and 20 are at the same level, 674 and 655 m^2/g, respectively. With the growth of CNTs during the CVD process, the strong adsorption in the low-pressure range significantly reduces in Ni-N-CNS/CNT-*X* samples (Figure 4b), indicating the disappearance of micropores, probably due to the deposited carbon filling into these pores. The samples with grown CNTs have similar specific surface areas, at 430, 384, and 441 m^2/g for 5, 20, and 60 min, respectively, and the reason that they are smaller than those of Ni-N-CNS-*Y* samples is probably because of denser CNTs growing during the CVD process since the commercial CNT with similar tube diameter (Figure S5c) showed a much smaller BET surface area, 101 m^2/g. Raman spectroscopy (Figure 4c) reveals two peaks at 1353 and 1580 cm^{-1}, corresponding to the disordered carbon (D band) and graphitic carbon (G band). The intensity ratio between these two bands (I_D/I_G) refers to the defect level of the materials.[56,57] With the growth of CNTs, the ratio of I_D/I_G in Ni-N-CNS/CNT-5 (1.25) and Ni-N-CNS/CNT-20 (1.24) was slightly larger than that in Ni-N-CNS-0 (1.15). This is probably caused by the defect-rich as-grown CNTs from the CVD process where arms or helical architecture could be observed in the SEM/TEM images representing more defects.[58] Compared to regular carbon structures, these defects may facilitate the formation of active sites generally believed to be Ni-N_x anchored in the carbon matrix.[59−61] Ni-N-CNS/CNT-60 showed a smaller I_D/I_G, 1.10, than the other groups, probably due to the complete graphitization and aggregation with a longer time of pyrolysis. Ni-N-CNS-20 showed a similar I_D/I_G, 1.16, to that of Ni-N-CNS-0, further confirming the contribution of CNT growth to the carbon defects in the materials.

The surface compositions and chemical states were investigated by X-ray photoelectron spectroscopy (XPS). The survey spectra (Figure S6) of Ni-N-CNS-0 and Ni-N-CNS/CNT-*X* display all C, N, O, and Ni peaks. The high-resolution C 1s spectrum of NiO-pC_3N_4 (Figure S7) displays two peaks of binding energy values at 284.8 and 287.8 eV corresponding to the graphite carbon and sp^2-bonded carbon in pC_3N_4, respectively.[62] However, only the peak at 284.8 eV was observed in the spectra of Ni-N-CNS and Ni-N-CNS/CNT-*X* (Figure S7), confirming the decomposition of pC_3N_4 and the release of N species during the CVD process. As shown in Figure S9, the high-resolution N 1s spectrum of NiO-pC_3N_4 reveal the nitrogen composition consisting of pyridinic N (398.3 eV), Ni-N (399.5 eV), pyrrolic N (400.5 eV), graphitic N (401.3 eV), and oxidized N (403 eV).[19,63−65] The pyridinic N peak dominates the nitrogen composition of NiO-pC_3N_4 indicating the uniform distribution of the sp^2-hybridized

https://doi.org/10.1021/acscatal.1c01864
ACS Catal. 2021, 11, 10333−10344

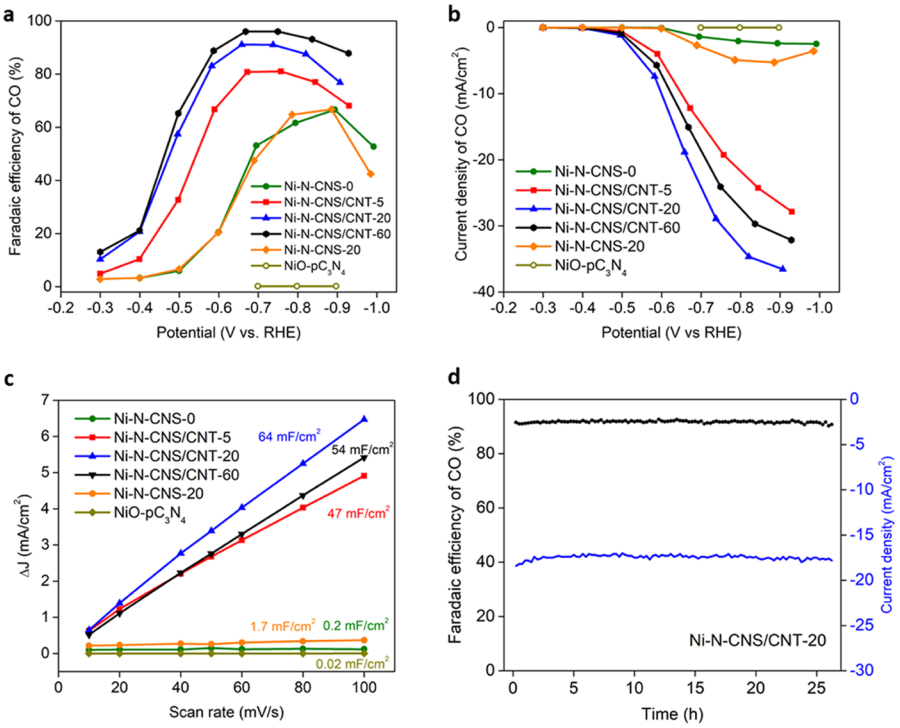

Figure 5. Electrochemical CO_2 reduction activity. (a) Faradaic efficiency of CO, (b) CO partial current density, and (c) charging current density differences plotted against scan rates of NiO-pC_3N_4, Ni-N-CNS-*Y*, and Ni-N-CNS/CNT-*X*. (d) CO_2RR stability of Ni-N-CNS/CNT-20 at −0.66 V vs RHE.

aromatic N bonded to carbon atoms, a typical pC_3N_4 structure.[66] The N 1s spectra of Ni-N-CNS-0 and Ni-N-CNS/CNT-*X* (Figure S9) and Ni-N-CNS-20 (Figure S8) also reveal the formation of these N species, indicating N doping after the CVD process. It is possible that these N species were derived from the decomposed pC_3N_4 and those evaporated and redeposited on the CNT surface, thus creating Ni-N_x active sites on both CNS and CNT. The percentage of different N species is listed in Table S2, and the increase of bulk-hosted graphitic N with CVD time suggests the decomposition of pC_3N_4 and the formation of CNTs. This is also confirmed by the surface element composition measured by XPS in Table S3, where N surface contents decrease while C contents increase with the CVD time. Moreover, Ni-N-CNS/CNT-20 has more C and fewer N contents than that of Ni-N-CNS-20, further suggesting the CNT growth from the C_2H_2 dissociation. The Ni atomic contents measured by XPS are 0.8, 0.5, 0.4, and 0.2 at. %, for Ni-N-CNS-0 and Ni-N-CNS/CNT-5, 20, and 60, respectively. Also, the Ni-N-CNS-20 sample has 0.6 at. % Ni, larger than that in Ni-N-CNS/CNT-20 (0.4 at. %). Because XPS as a surface characterization technique has a detection depth less than 5 nm,[67] this trend of decreasing Ni content with longer CVD time suggests that Ni particles are encapsulated by CNTs, agreeing with the observations from TEM analyses (Figure 3b). The Ni content of Ni-N-CNS/CNT-20 detected by ICP is 5.2 wt %, much larger than that from XPS (1.9 wt %), further confirming the encapsulation of Ni nanoparticles. In addition, the binding energies of Ni $2p_{3/2}$ in Ni-N-CNS-0 and Ni-N-CNS/CNT-*X* (Figure 4d) all have an obvious shift toward higher values compared to Ni metal,[19,23] suggesting that the majority of the surface Ni oxidation state was counted from the Ni-N site instead of wrapped Ni nanoparticles.

More details on the chemical environment and atomic coordination of Ni atoms were revealed by X-ray absorption spectroscopy (XAS). Ni foil, nickel phthalocyanine (NiPc), and nickel oxide (NiO) were also tested as standard references. X-ray absorption near-edge structure spectroscopy (XANES) in Figure 4e shows that the rising edges of Ni-N-CNS/CNT-20 are very close to Ni foil (Ni^0) indicating the dominance of metallic Ni, formed in the reducing environment during the catalyst synthesis.[68] The rising edges of Ni-N-CNS/CNT-20 show a slight shift toward NiO (Ni^{2+}) probably due to the presence of Ni-N active sites in which the electrons are attracted toward the neighboring heterodoped atoms such as N, in agreement with XPS results, where Ni peaks also possess a shift away from Ni^0 (Figure 4d).[69] Fourier transform (FT) extended X-ray absorption fine structure (EXAFS) was further carried out to analyze the atomic-level structure. As shown in Figure 4f, Ni-N-CNS/CNT-20 has two prominent peaks at around 1.4 and 2.2 Å, which can be ascribed to the Ni-N and Ni-Ni coordinations, confirmed by the same positions of Ni-N in NiPc and Ni-Ni in the Ni foil. No pronounced Ni−O peak was observed. These results indicate that both Ni-N sites and the Ni nanoparticle structure are present in the catalyst system. Although the exact coordination number of Ni-N and Ni-Ni cannot be determined reliably by fitting because of the coexistence of Ni nanoparticles and single atomic Ni, the XAS characterizations confirm the presence of both Ni-N active sites and encapsulated Ni nanoparticles in the CNS/CNT hybrid system synthesized by the CVD pyrolysis method in this work.

Fourier-transformed EXAFS spectra of Ni-N-CNS/CNT-20 and Ni-N-CNS-20 are further compared. Even though the exact coordination number cannot be obtained by fitting, the peak intensity tells the difference in the coordination number qualitatively. Because of the similar intensity of the Ni-N peak

https://doi.org/10.1021/acscatal.1c01864
ACS Catal. 2021, 11, 10333−10344

(1.4 Å) (Figure S10a), the coordination number of Ni in the Ni-N structure in these two samples should be similar. A broader Ni-N peak in the Ni-N-CNS/CNT-20 EXAFS spectra compared to that in the Ni-N-CNS-20 EXAFS spectra means a larger disorder degree. The larger intensity of the Ni-Ni peak (2.2 Å) of Ni-N-CNS-20 reveals a larger coordination number in Ni nanoparticles or a larger Ni particle size. This suggests that the subsequent growth of CNTs on Ni nanoparticles (to form Ni-N-CNS/CNT-20) will lead to the spread of Ni contents, i.e., the formation of atomic Ni sites along the length of the CNT. Moreover, the pre-edge and absorption edge of Ni-N-CNS/CNT-20 shift to a higher energy region compared with that of Ni-N-CNS-20 (Figure S10b,c), meaning that the average oxidation state of Ni in Ni-N-CNS/CNT-20 is a little bit higher. This further demonstrates more unsaturated Ni-N_x ($x < 4$) sites and/or smaller Ni nanoparticle sizes in Ni-N-CNS/CNT-20.

3.2. Evaluation of CO_2RR Activity. *3.2.1. H-Cell Electrolysis: Structure−Performance Correlation.* The electrochemical CO_2 reduction performance was evaluated in a three-electrode H-cell reactor. The significant increase of the linear sweep voltammetry (LSV) results recorded in the CO_2-saturated 0.5 M $KHCO_3$ electrolyte compared to that in Ar-saturated solution indicates the occurrence of the CO_2RR (Figure S11). No liquid product was detected by NMR as shown in Figure S12. The Faradaic efficiency of CO (FE(CO)), the total current densities (J), and the CO partial current densities (J_{CO}) are revealed in Figure 5a, Figure S13, and Figure 5b, respectively. NiO-pC_3N_4 shows almost no CO_2RR activity with FE(CO) of only around 0.2%, indicating that the Ni-N active sites did not form during the precursor preparation. Ni-N-CNS-*Y* also show sluggish CO_2RR activity in terms of CO current densities with only 1.4 and 2.7 mA/cm^2 at −0.69 V (vs RHE) and FE(CO) values of 53 and 47% for the 0 and 20 min samples, respectively, suggesting that few active sites were formed without the CVD process. With only 5 min CVD growth, Ni-N-CNS/CNT-5 presents a much larger CO current density, 12.2 mA/cm^2 at −0.67 V, and an FE(CO) of 81%. Ni-N-CNS/CNT-20 has a further increased J_{CO}, 18.9 mA/cm^2 at −0.66 V with 90% FE(CO) and 28.9 mA/cm^2 at −0.74 V with 91% FE(CO). Ni-N-CNS/CNT-60 exhibits the highest CO selectivity of 96% at −0.67 V with a slightly smaller J_{CO}, 15.1 mA/cm^2. The significantly higher J_{CO} and FE(CO) of Ni-N-CNS/CNT-*X* samples than those of Ni-N-CNS-*Y* indicate that the majority of the active sites were formed during the CVD process. Results of repeated tests for Ni-N-CNS/CNT-20 and Ni-N-CNS-20 (Figure S14) indicate good repeatability of the H-cell experiments.

Electrochemistry characterizations are carried out to further investigate the electrochemical property of each sample. As revealed by the electrochemical impedance spectroscopy (EIS) in Figure S15a, Ni-N-CNS-0 and all Ni-N-CNS/CNT-*X* samples have about two orders of magnitude smaller charge transfer resistance (semicircle diameter in a Nyquist plot) than that of NiO-pC_3N_4, indicating a better electron transfer capability from the catalyst to the electrolyte, while the three samples with CNT growth (Ni-N-CNS/CNT-*X*) show a further reduced charge transfer resistance than Ni-N-CNS-0, with the smallest resistance observed in Ni-N-CNS/CNT-20. The comparison between Ni-N-CNS/CNT-20 and the CNT-free counterpart Ni-N-CNS-20 in Figure S15b demonstrates a lower charge transfer resistance in Ni-N-CNS/CNT-20. In addition, the double-layer capacitances (C_{dl}) of all the samples are compared in Figure 5c. The C_{dl} was obtained by cyclic voltammetry (CV) in a non-Faradaic potential range from 0 to 0.3 V vs RHE (Figure S16a−f) and calculated by using the slope of the plots of current density differences as a function of applied scanning rates. Ni-N-CNS/CNT-20 had the highest C_{dl} value, 64 mF/cm^2, indicating the highest electrochemical surface area (ECSA), as ECSA is positively proportional to C_{dl}. Ni-N-CNS-0, Ni-N-CNS/CNT-5, and Ni-N-CNS/CNT-60 had C_{dl} values at 0.2, 47, and 54 mF/cm^2, respectively. The variations of the ECSA among the samples correlate well with those of the CO current density, confirming that Ni-N-CNS/CNT-20 possesses the highest active site density among all groups. The CNT-free sample Ni-N-CNS-20 showed a much lower C_{dl} (1.7 mF/cm^2) than that of Ni-N-CNS/CNT-20 (64 mF/cm^2). The J_{CO} values normalized by the ECSA (J_{CO}/ECSA) are calculated. Interestingly, Ni-N-CNS-*Y* samples have a larger J_{CO}/ECSA than Ni-N-CNS/CNT-*X* (Figure S17a), while J_{CO}/ECSA values are similar within Ni-N-CNS/CNT-*X* samples (Figure S17b). However, due to the larger ECSA (more electrochemically active sites) and lower charge transfer resistance of Ni-N-CNS/CNT-*X* in comparison to Ni-N-CNS-*Y*, the CO_2RR performances of Ni-N-CNS/CNT-*X* are much higher. This result indirectly demonstrates the advantage of the 3D hybrid CNS/CNT structure. The long-term stability measurement in Figure 5d shows a stable electrolysis in terms of both FE(CO) and current density for 26 h without an obvious decrease.

As confirmed by the SEM/TEM images, the CNTs grown in Ni-N-CNS/CNT-*X* linked the CNS layers and formed a 3D hierarchical structure. The highly conductive nature of CNTs significantly reduces the charge transfer resistance and exposes more electrochemical active surface areas than those of Ni-N-CNS-*Y* as determined by the electrochemical characterizations. XAS and HAADF-STEM reveal the Ni-N bonds and atomic Ni sites, respectively, which are generally accepted as the active sites for the CO_2RR in previous studies.[19,20,23] However, a longer CVD process will result in more N elements released due to the decomposition of pC_3N_4 as evidenced by XPS, resulting in less potential N sources to form Ni-N active sites. The balance among the charge transfer resistance, electrochemical active surface area, and the nitrogen content loss led to the current density first increasing then decreasing with a longer CVD process, with the highest value being observed in Ni-N-CNS/CNT-20.

To further understand the structure−performance relationship, the materials' property and performance of Ni-N-CNS/CNT-20 were compared to Ni-N-CSN/CNT-20-acid, which was synthesized by washing Ni-N-CNS/CNT-20 with HCl for 24 h. As shown in Figure S18a, Ni-N-CNS/CNT-20 and Ni-N-CNS/CNT-20-acid achieved similar FE for CO, which suggests that most of the Ni NPs are encapsulated by carbon layers and thus not washed out by acid; otherwise, the FE(CO) would have been higher for the acid-washed one since Ni NPs favor the HER.[10,70,71] Ni-N-CNS/CNT-20-acid shows a slight decrease in CO current compared to that of Ni-N-CNS/CNT-20 (Figure S18b) possibly due to the generation of a small quantity of oxygen functional groups during the acid wash,[72] which reduces the charge transfer resistance as shown in Figure S18c. TEM images of Ni-N-CNS/CNT-20-acid (Figure S18d,e) show a similar structure to that of Ni-N-CNS/CNT-20 with clear Ni NPs remaining after acid wash. Further HR-TEM imaging of a Ni nanoparticle in Ni-N-CNS/CNT-20-acid (Figure S18f) confirms that the encapsulation by

https://doi.org/10.1021/acscatal.1c01864
ACS Catal. 2021, 11, 10333−10344

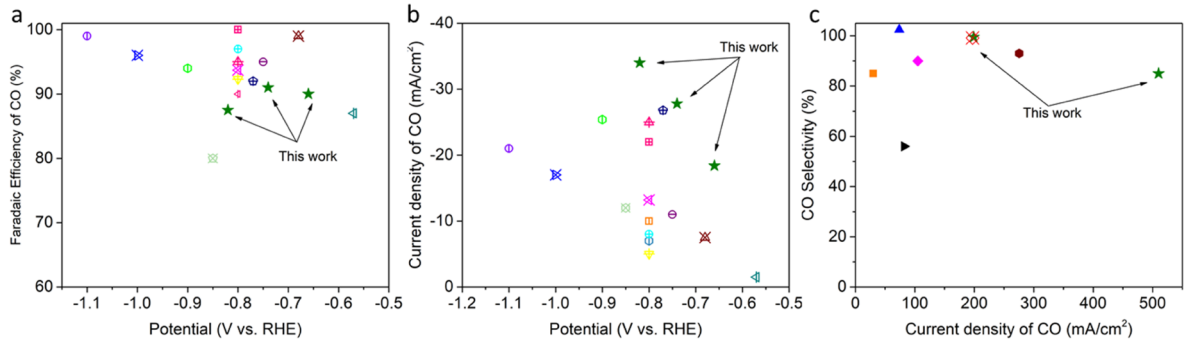

Figure 6. Comparisons of the CO_2RR performance of this work with those in the literature: (a, b) H-cell performance and (c) flow cell performance (detailed comparisons of experimental conditions and performances are listed in Tables S4 and S5).

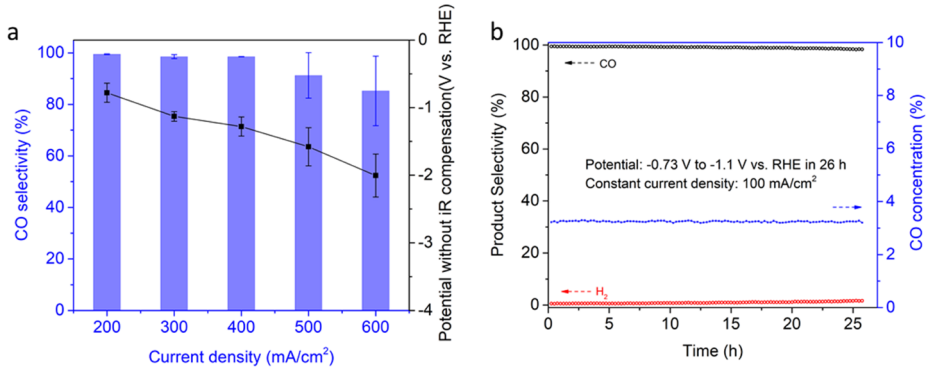

Figure 7. (a) CO_2RR performance measured in a flow cell and (b) the result of a 26 h flow cell stability test.

carbon layers was well preserved after acid washing. This encapsulation blocks Ni nanoparticles from contacting the reactants during electrolysis, which results in the high selectivity of CO in Ni-N-CNS/CNT-20 even if Ni nanoparticles and atomic sites coexist in the system.

In order to prepare a sample of only CNTs as a comparison to further investigate the role CNT and CNS play in the hybrid system, Ni-N-melamine-20 was prepared by 20 min CVD using the same procedure except eliminating the pre-polymerization of melamine to pC_3N_4. From the SEM images of Ni-N-melamine-20 in Figure S19, the sample is dominated by larger diameter CNTs without an obvious CNS structure, which is different from that of Ni-N-CSN/CNT-20 (Figure S19a). Similar morphologies were observed in the previous studies, where the pyrolysis of melamine and CNTs will only result in a tube-structure material.[73,74] This is probably because melamine is less thermally stable and decomposed more rapidly than pC_3N_4, as a result of which the layer substrate was difficult to form.[75,76] As shown in Figure S20, the CNT-dominant sample Ni-N-melamine-20 has a higher FE(CO) than that of Ni-N-CNS/CNT-20, 97% vs 90% at −0.66 V. However, the current density of CO in Ni-N-melamine-20 was significantly lower, at 9.0 mA/cm^2 vs 18.9 mA/cm^2 for Ni-N-CNS/CNT-20. This could be resulted by a better Ni element distribution and less Ni nanoparticle formation without the 2 h pre-polymerization treatment in air. However, the lack of a 3D hierarchical structure eliminates the advantages that Ni-N-CNS/CNT-20 possesses, making the current density of Ni-N-melamine-20 lower. The results indicate the significance of pre-polymerization of melamine and the formation of pC_3N_4. Forming a layer substrate by pre-polymerization is essential to the hierarchical structure and CO_2RR performance.

The correlation between the characterizations and performance suggests that with the growth of CNT and generation of CNS, the hybrid system possesses high CO_2RR catalytic activity and selectivity, placing it among the top ones in the Ni-N-C catalysts reported in the literature. As shown in Table S4, the 5 min and 60 min CVD samples in this work already show comparable CO_2RR performance to the previous reports. For the 20 min CVD sample, the average CO current density reaches 18.4 and 27.8 mA/cm^2 at −0.66 and − 0.74 V, respectively, making Ni-N-CNS/CNT-20 achieve one of the best activities among the top-tier literature under the same electrolysis conditions (Figure 6a,b). Compared to conventional 1D or 2D-structured M-N-C catalysts, the 3D CNT/CNS hierarchical structure developed in this work possesses a better mass transfer rate and higher conductivity, and the synthesis requires less pyrolysis time, lower temperature, and no additional treatment, suggesting a more energy efficient and cost-effective method.

3.2.2. Flow Cell Electrolysis. As revealed in Figure 7a, the CO selectivity remained above 80% at a wide range of current densities, from 200 to 600 mA/cm^2. In average, the CO selectivity was 99.5% at 200 mA/cm^2 current density (J_{CO} = 199 mA/cm^2) and 85% at 600 mA/cm^2 (J_{CO} = 510 mA/cm^2), indicating an excellent catalytic performance that is suitable for commercial applications.[49] In general, as the input current density increases, the required potential is larger and the experimental uncertainty becomes larger as well, likely due to the increased sensitivity to flow cell operation parameters.

The stability of the CO_2RR in a flow cell was tested at different current densities for longer hours. First, the stability test was performed at 300 mA/cm^2 for 8 h, and the result is shown in Figure S21a. A certain increase in H_2 selectivity and

https://doi.org/10.1021/acscatal.1c01864
ACS Catal. 2021, 11, 10333−10344

decrease of CO selectivity and a slight decrease of the CO concentration in the effluent gas were observed over time, while the cathode potential also increased from −0.9 to −1.0 V after 8 h. According to the studies,[77,78] the generation of (bi)carbonates is still one of the biggest challenges in CO_2RR flow cell research, especially at high current densities. The (bi)carbonates may block the catalyst/CO_2/catholyte interface, limit the access of CO_2 to the catalyst, and make the electrode more hydrophilic, resulting in degradation in the long-term test. To further probe the origin of the instability (since the performance is very stable in the H-cell performance as shown in Figure 5d), the catholyte was changed with fresh KOH twice at 4.5 and 6.5 h. With each KOH change, a sharp decrease in H_2 selectivity is observed (Figure S21a). This approach, which is frequently used in the research field,[79,80] suggests the effectiveness of suppressing the HER by refreshing the electrolyte and removing the generated (bi)carbonates. The concentration of produced CO measured at the cell effluent remained stable at around 3% with no signs of degradation during the 26 h test.

To further explore the long-term stability without the need to refresh the electrolyte, a 26 h stability test was performed at a lower current density, 100 mA/cm^2, which is still considered as a commercially viable current density. As shown in Figure 7b, the CO selectivity in the final products slightly decreased from 99.5 to 98.3% during the reaction, while the selectivity of H_2 slightly increased from 0.5 to 1.7%. The pH decreased from 14 to 11 (Figure S21b), indicating the generation of (bi)carbonates. Consequently, the resistance of the system increased because of the decreased OH^- concentration, which also results in a gradual potential increase over 26 h from −0.73 to −1.1 V.[77,78]

Results from the stability tests at the two different current densities (300 and 100 mA/cm^2) suggest the trade-off between current and stability, which should be the future research focus in the community for scale-up studies. Overall, the CO_2RR performances in both H-cell and flow cell setups obtained in this work are among the few highest ones in the literature by M-N-C catalysts in terms of current density and CO selectivity, as shown in Figure 6. Detailed comparisons of experimental conditions and performances are listed in Tables S4 and S5. In addition, the flow cell tests of Ni-N-CNS/CNT-20 show a much higher activity than a traditional Ag/C catalyst (Figure S22) and better stability than the CNT-structured Ni-N-melamine (Figure S23) in the same flow cell setup, further confirming the advantageous 3D CNT/CNS structure of Ni-N-CNS/CNT-20.

4. CONCLUSIONS

In summary, we demonstrated an approach of chemical vapor deposition to prepare highly efficient hybrid carbon nanotube and nanosheet catalysts for a CO_2RR. The hierarchical structure of CNT and CNS (e.g., Ni-N-CNS/CNT-20) provides a high electrochemical surface area and less charge transfer resistance than either the CNT-free (Ni-N-CNS-20) or CNT-dominant (Ni-N-melamine-20) samples. Although both Ni-N active sites and Ni nanoparticles are formed on the catalysts, carbon layers grown during the CVD process encapsulate the Ni nanoparticles and suppress the competing hydrogen evolution reaction. The as-prepared Ni-N-CNS/CNT-*X* catalysts exhibit highly efficient CO_2RR activity with more than 90% FE(CO). Ni-N-CNS/CNT-20 showed the topmost level of activities in the reported Ni-N-C catalysts, achieving stable CO partial current densities of 18.9 and 28.9 mA/cm^2 with FE(CO) values of 90 and 91% at −0.66 and −0.74 V, respectively, in an H-cell setup. The catalyst also achieved a commercially viable current density at 600 mA/cm^2 in a flow cell with 85% CO selectivity. By taking the advantages of the hierarchical CNS/CNT structure that is composed of highly active Ni-N active sites while encapsulating Ni nanoparticles, the CO_2RR performance in both H-cell and flow cell obtained in this work reached one of the best in the literature in terms of both current density and CO selectivity in the field of M-N-C catalysts.

■ ASSOCIATED CONTENT

Supporting Information

The Supporting Information is available free of charge at https://pubs.acs.org/doi/10.1021/acscatal.1c01864.

Selectivity calculation, cell schematic, additional results of SEM, TEM, XPS, BET, and NMR characterizations, additional results of CO2RR activity, and performance comparison (PDF)

■ AUTHOR INFORMATION

Corresponding Author

Ying Li − *J. Mike Walker '66 Department of Mechanical Engineering, Texas A&M University, College Station, Texas 77843, United States;* orcid.org/0000-0002-6775-5649; Email: yingli@tamu.edu

Authors

Yang Gang − *J. Mike Walker '66 Department of Mechanical Engineering, Texas A&M University, College Station, Texas 77843, United States*

Erik Sarnello − *Department of Chemistry and Biochemistry, Northern Illinois University, DeKalb, Illinois 60115, United States*

John Pellessier − *J. Mike Walker '66 Department of Mechanical Engineering, Texas A&M University, College Station, Texas 77843, United States*

Siyuan Fang − *Department of Materials Science and Engineering, Michigan Technological University, Houghton, Michigan 49931, United States;* orcid.org/0000-0002-1439-3365

Manuel Suarez − *J. Mike Walker '66 Department of Mechanical Engineering, Texas A&M University, College Station, Texas 77843, United States*

Fuping Pan − *J. Mike Walker '66 Department of Mechanical Engineering, Texas A&M University, College Station, Texas 77843, United States;* orcid.org/0000-0001-9171-0726

Zichen Du − *J. Mike Walker '66 Department of Mechanical Engineering, Texas A&M University, College Station, Texas 77843, United States;* orcid.org/0000-0002-0231-6944

Peng Zhang − *Department of Chemistry, Texas A&M University, College Station, Texas 77843, United States;* orcid.org/0000-0003-0973-1523

Lingzhe Fang − *Department of Chemistry and Biochemistry, Northern Illinois University, DeKalb, Illinois 60115, United States*

Yuzi Liu − *Center of Nanoscale Materials, Argonne National Laboratory, Lemont, Illinois 60439, United States;* orcid.org/0000-0002-8733-1683

Tao Li − *Department of Chemistry and Biochemistry, Northern Illinois University, DeKalb, Illinois 60115, United*

States; Chemistry and Material Science Group, X-ray Science Division, Argonne National Laboratory, Lemont, Illinois 60439, United States; orcid.org/0000-0002-4913-4486

Hong-Cai Zhou − *Department of Chemistry, Texas A&M University, College Station, Texas 77843, United States;* orcid.org/0000-0002-9029-3788

Yun Hang Hu − *Department of Materials Science and Engineering, Michigan Technological University, Houghton, Michigan 49931, United States;* orcid.org/0000-0002-5358-8667

Complete contact information is available at: https://pubs.acs.org/10.1021/acscatal.1c01864

Notes

The authors declare no competing financial interest.

■ ACKNOWLEDGMENTS

This work was supported by the U.S. National Science Foundation (NSF CBET #1805132). The use of the Materials Characterization Facility (MCF) at Texas A&M University is acknowledged. The use of the Advanced Photon Source, Office of Science User Facility, operated for the U.S. Department of Energy (DOE) Office of Science by Argonne National Laboratory is supported by the U.S. DOE under contract DE-AC02-06CH11357.

■ REFERENCES

(1) Jones, J.-P.; Prakash, G. K. S.; Olah, G. A. Electrochemical CO_2 reduction: recent advances and current trends. *Isr. J. Chem.* **2014**, *54*, 1451−1466.

(2) West, J. J.; Smith, S. J.; Silva, R. A.; Naik, V.; Zhang, Y.; Adelman, Z.; Fry, M. M.; Anenberg, S.; Horowitz, L. W.; Lamarque, J. F. Co-benefits of Global Greenhouse Gas Mitigation for Future Air Quality and Human Health. *Nat. Clim. Change* **2013**, *3*, 885−889.

(3) Rochelle, G. T. Amine scrubbing for CO_2 capture. *Science* **2009**, *325*, 1652−1654.

(4) Bates, E. D.; Mayton, R. D.; Ntai, I.; Davis, J. H. CO_2 capture by a task-specific ionic liquid. *J. Am. Chem. Soc.* **2002**, *124*, 926−927.

(5) Rafiee, A.; Khalilpour, K. R.; Milani, D.; Panahi, M. Trends in CO_2 conversion and utilization: A review from process systems perspective. *J. Environ. Chem. Eng.* **2018**, *6*, 5771−5794.

(6) Pan, F.; Deng, W.; Justiniano, C.; Li, Y. Identification of champion transition metals centers in metal and nitrogen-codoped carbon catalysts for CO_2 reduction. *Appl. Catal., B* **2018**, *226*, 463−472.

(7) Pan, F.; Zhang, H.; Liu, K.; Cullen, D.; More, K.; Wang, M.; Feng, Z.; Wang, G.; Wu, G.; Li, Y. Unveiling Active Sites of CO_2 Reduction on Nitrogen-Coordinated and Atomically Dispersed Iron and Cobalt Catalysts. *ACS Catal.* **2018**, *8*, 3116−3122.

(8) Pan, Y.; Lin, R.; Chen, Y.; Liu, S.; Zhu, W.; Cao, X.; Chen, W.; Wu, K.; Cheong, W.-C.; Wang, Y.; Zheng, L.; Luo, J.; Lin, Y.; Liu, Y.; Liu, C.; Li, J.; Lu, Q.; Chen, X.; Wang, D.; Peng, Q.; Chen, C.; Li, Y. Design of Single-Atom Co-N5 Catalytic Site: A Robust Electrocatalyst for CO_2 Reduction with Nearly 100% CO Selectivity and Remarkable Stability. *J. Am. Chem. Soc.* **2018**, *140*, 4218−4221.

(9) Pan, F.; Zhang, H.; Liu, Z.; Cullen, D.; Liu, K.; More, K.; Wu, G.; Wang, G.; Li, Y. Atomic-level active sites of efficient imidazolate framework-derived nickel catalysts for CO_2 reduction. *J. Mater. Chem. A* **2019**, *7*, 26231−26237.

(10) Pan, F.; Li, B.; Sarnello, E.; Hwang, S.; Gang, Y.; Feng, X.; Xiang, X.; Adli, N. M.; Li, T.; Su, D.; Wu, G.; Wang, G.; Li, Y. Boosting CO_2 reduction on Fe-NC with sulfur incorporation: Synergistic electronic and structural engineering. *Nano Energy* **2020**, *68*, 104384.

(11) Liu, S.; Yang, H.; Huang, X.; Liu, L.; Cai, W.; Gao, J.; Li, X.; Zhang, T.; Huang, Y.; Liu, B. Identifying Active Sites of Nitrogen-Doped Carbon Materials for the CO_2 Reduction Reaction. *Adv. Funct. Mater.* **2018**, *28*, 1800499.

(12) Ju, W.; Bagger, A.; Hao, G.-P.; Varela, A. S.; Sinev, I.; Bon, V.; Cuenya, B. R.; Kaskel, S.; Rossmeisl, J.; Strasser, P. Understanding activity and selectivity of metal-nitrogen-doped carbon catalysts for electrochemical reduction of $CO0_2$. *Nat. Commun.* **2017**, *8*, 944.

(13) Zhang, C.; Yang, S.; Wu, J.; Liu, M.; Yazdi, S.; Ren, M.; Sha, J.; Zhong, J.; Nie, K.; Jalilov, A. S.; Li, Z.; Li, H.; Yakobson, B. I.; Wu, Q.; Ringe, E.; Xu, H.; Ajayan, P. M.; Tour, J. M. Electrochemical CO_2 Reduction with Atomic Iron-Dispersed on Nitrogen-Doped Graphene. *Adv. Energy Mater.* **2018**, *8*, 1703487.

(14) Duan, X.; Xu, J.; Wei, Z.; Ma, J.; Guo, S.; Wang, S.; Liu, H.; Dou, S. Metal-Free Carbon Materials for CO_2 Electrochemical Reduction. *Adv. Mater.* **2017**, *29*, 1701784.

(15) Ma, T.; Fan, Q.; Li, X.; Qiu, J.; Wu, T.; Sun, Z. Graphene-based materials for electrochemical CO_2 reduction. *J. CO2 Util.* **2019**, *30*, 168−182.

(16) Cheng, Y.; Zhao, S.; Johannessen, B.; Veder, J.-P.; Saunders, M.; Rowles, M. R.; Cheng, M.; Liu, C.; Chisholm, M. F.; De Marco, R.; Cheng, H.-M.; Yang, S.-Z.; Jiang, S. P. Atomically Dispersed Transition Metals on Carbon Nanotubes with Ultrahigh Loading for Selective Electrochemical Carbon Dioxide Reduction. *Adv. Mater.* **2018**, *30*, No. e1706287.

(17) Pan, F.; Zhao, H.; Deng, W.; Feng, X.; Li, Y. A novel N, Fe-Decorated carbon nanotube/carbon nanosheet architecture for efficient CO_2 reduction. *Electrochim. Acta* **2018**, *273*, 154−161.

(18) Georgakilas, V.; Tiwari, J. N.; Kemp, K. C.; Perman, J. A.; Bourlinos, A. B.; Kim, K. S.; Zboril, R. Noncovalent Functionalization of Graphene and Graphene Oxide for Energy Materials, Biosensing, Catalytic, and Biomedical Applications. *Chem. Rev.* **2016**, *116*, 5464−5519.

(19) Zheng, T.; Jiang, K.; Ta, N.; Hu, Y.; Zeng, J.; Liu, J.; Wang, H. Large-Scale and Highly Selective CO_2 Electrocatalytic Reduction on Nickel Single-Atom Catalyst. *Joule* **2019**, *3*, 265−278.

(20) Lu, P.; Yang, Y.; Yao, J.; Wang, M.; Dipazir, S.; Yuan, M.; Zhang, J.; Wang, X.; Xie, Z.; Zhang, G. Facile synthesis of single-nickel-atomic dispersed N-doped carbon framework for efficient electrochemical CO_2 reduction. *Appl. Catal., B* **2019**, *241*, 113−119.

(21) Wu, J.; Yadav, R. M.; Liu, M.; Sharma, P. P.; Tiwary, C. S.; Ma, L.; Zou, X.; Zhou, X.-D.; Yakobson, B. I.; Lou, J.; Ajayan, P. M. Achieving highly efficient, selective, and stable CO_2 reduction on nitrogen-doped carbon nanotubes. *ACS Nano* **2015**, *9*, 5364−5371.

(22) Pan, F.; Li, B.; Sarnello, E.; Fei, Y.; Gang, Y.; Xiang, X.; Du, Z.; Zhang, P.; Wang, G.; Nguyen, H. T.; Li, T.; Hu, Y. H.; Zhou, H.-C.; Li, Y. Atomically Dispersed Iron-Nitrogen Sites on Hierarchically Mesoporous Carbon Nanotube and Graphene Nanoribbon Networks for CO_2 Reduction. *ACS Nano* **2020**, *14*, 5506−5516.

(23) Zhao, C.; Wang, Y.; Li, Z.; Chen, W.; Xu, Q.; He, D.; Xi, D.; Zhang, Q.; Yuan, T.; Qu, Y.; Yang, J.; Zhou, F.; Yang, Z.; Wang, X.; Wang, J.; Luo, J.; Li, Y.; Duan, H.; Wu, Y.; Li, Y. Solid-Diffusion Synthesis of Single-Atom Catalysts Directly from Bulk Metal for Efficient CO_2 Reduction. *Joule* **2019**, *3*, 584−594.

(24) Yu, K.; Lu, G.; Bo, Z.; Mao, S.; Chen, J. Carbon Nanotube with Chemically Bonded Graphene Leaves for Electronic and Optoelectronic Applications. *J. Phys. Chem. Lett.* **2011**, *2*, 1556−1562.

(25) Lv, R.; Cui, T.; Jun, M.-S.; Zhang, Q.; Cao, A.; Su, D. S.; Zhang, Z.; Yoon, S.-H.; Miyawaki, J.; Mochida, I.; Kang, F. Open-Ended, N-Doped Carbon Nanotube-Graphene Hybrid Nanostructures as High-Performance Catalyst Support. *Adv. Funct. Mater.* **2011**, *21*, 999−1006.

(26) Liang, H.-W.; Zhuang, X.; Brüller, S.; Feng, X.; Müllen, K. Hierarchically porous carbons with optimized nitrogen doping as highly active electrocatalysts for oxygen reduction. *Nat. Commun.* **2014**, *5*, 4973.

(27) Melke, J.; Schuster, R.; Möbus, S.; Jurzinsky, T.; Elsässer, P.; Heilemann, A.; Fischer, A. Electrochemical stability of silica-templated polyaniline-derived mesoporous N-doped carbons for the design of Pt-based oxygen reduction reaction catalysts. *Carbon* **2019**, *146*, 44−59.

(28) Han, A.; Wang, B.; Kumar, A.; Qin, Y.; Jin, J.; Wang, X.; Yang, C.; Dong, B.; Jia, Y.; Liu, J.; Sun, X. Recent advances for MOF-derived carbon-supported single-atom catalysts. *Small Methods* **2019**, *3*, 1800471.
(29) Zhu, Y.; Li, L.; Zhang, C.; Casillas, G.; Sun, Z.; Yan, Z.; Ruan, G.; Peng, Z.; Raji, A.-R. O.; Kittrell, C.; Hauge, R. H.; Tour, J. M. A seamless three-dimensional carbon nanotube graphene hybrid material. *Nat. Commun.* **2012**, *3*, 1225.
(30) Yan, X.-L.; Li, H.-F.; Wang, C.; Jiang, B.-B.; Hu, H.-Y.; Xie, N.; Wu, M. H.; Vinodgopal, K.; Dai, G.-P. Melamine as a single source for fabrication of mesoscopic 3D composites of N-doped carbon nanotubes on graphene. *RSC Adv.* **2018**, *8*, 12157−12164.
(31) Wang, D.; Ma, Z.; Xie, Y.'e.; Zhang, M.; Zhao, N.; Song, H. Fe/N-doped graphene with rod-like CNTs as an air-cathode catalyst in microbial fuel cells. *RSC Adv.* **2018**, *8*, 1203−1209.
(32) Samad, Y. A.; Li, Y.; Schiffer, A.; Alhassan, S. M.; Liao, K. Graphene foam developed with a novel two-step technique for low and high strains and pressure-sensing applications. *Small* **2015**, *11*, 2380−2385.
(33) Cui, T.; Lv, R.; Huang, Z.-H.; Zhu, H.; Zhang, J.; Li, Z.; Jia, Y.; Kang, F.; Wang, K.; Wu, D. Synthesis of nitrogen-doped carbon thin films and their applications in solar cells. *Carbon* **2011**, *49*, 5022−5028.
(34) Thirumal, V.; Pandurangan, A.; Jayavel, R.; Krishnamoorthi, S. R.; Ilangovan, R. Synthesis of nitrogen doped coiled double walled carbon nanotubes by chemical vapor deposition method for supercapacitor applications. *Curr. Appl. Phys.* **2016**, *16*, 816−825.
(35) Kim, C.-d.; Lee, H.-R.; Kim, H. T. Effect of NH_3 gas ratio on the formation of nitrogen-doped carbon nanotubes using thermal chemical vapor deposition. *Mater. Chem. Phys.* **2016**, *183*, 315−319.
(36) Das, D.; Banerjee, D.; Mondal, M.; Shett, A.; Das, B.; Das, N. S.; Ghorai, U. K.; Chattopadhyay, K. K. Nickel doped graphitic carbon nitride nanosheets and its application for dye degradation by chemical catalysis. *Mater. Res. Bull.* **2018**, *101*, 291−304.
(37) Kessler, F. K.; Zheng, Y.; Schwarz, D.; Merschjann, C.; Schnick, W.; Wang, X.; Bojdys, M. J. Functional carbon nitride materials design strategies for electrochemical devices. *Nat. Rev. Mater.* **2017**, *2*, 17030.
(38) Xia, Y.; Mokaya, R. Synthesis of ordered mesoporous carbon and nitrogen-doped carbon materials with graphitic pore walls via a simple chemical vapor deposition method. *Adv. Mater.* **2004**, *16*, 1553−1558.
(39) Liu, J.; Webster, S.; Carroll, D. L. Highly aligned coiled nitrogen-doped carbon nanotubes synthesized by injection-assisted chemical vapor deposition. *Appl. Phys. Lett.* **2006**, *88*, 213119.
(40) Li, Y.; Wang, J.; Li, X.; Liu, J.; Geng, D.; Yang, J.; Li, R.; Sun, X. Nitrogen-doped carbon nanotubes as cathode for lithium-air batteries. *Electrochem. Commun.* **2011**, *13*, 668−672.
(41) Zhang, X. X.; Li, Z. Q.; Wen, G. H.; Fung, K. K.; Chen, J.; Li, Y. Microstructure and growth of bamboo-shaped carbon nanotubes. *Chem. Phys. Lett.* **2001**, *333*, 509−514.
(42) Kukovitsky, E. F.; L'vov, S. G.; Sainov, N. A.; Shustov, V. A.; Chernozatonskii, L. A. Correlation between metal catalyst particle size and carbon nanotube growth. *Chem. Phys. Lett.* **2002**, *355*, 497−503.
(43) Yoon, Y. J.; Baik, H. K. Catalytic growth mechanism of carbon nanofibers through chemical vapor deposition. *Diamond Relat. Mater.* **2001**, *10*, 1214−1217.
(44) Daiyan, R.; Lu, X.; Tan, X.; Zhu, X.; Chen, R.; Smith, S. C.; Amal, R. Antipoisoning nickel−carbon electrocatalyst for practical electrochemical CO_2 reduction to CO. *ACS Appl. Energy Mater.* **2019**, *2*, 8002−8009.
(45) Jia, M.; Choi, C.; Wu, T.-S.; Ma, C.; Kang, P.; Tao, H.; Fan, Q.; Hong, S.; Liu, S.; Soo, Y.-L.; Jung, Y.; Qiu, J.; Sun, Z. Carbon-supported Ni nanoparticles for efficient CO_2 electroreduction. *Chem. Sci.* **2018**, *9*, 8775−8780.
(46) Daiyan, R.; Chen, R.; Kumar, P.; Bedford, N. M.; Qu, J.; Cairney, J. M.; Lu, X.; Amal, R. Tunable syngas production through CO_2 electroreduction on cobalt−carbon composite electrocatalyst. *ACS Appl. Mater. Interfaces* **2020**, *12*, 9307−9315.
(47) Koshy, D. M.; Chen, S.; Lee, D. U.; Stevens, M. B.; Abdellah, A. M.; Dull, S. M.; Chen, G.; Nordlund, D.; Gallo, A.; Hahn, C.; Higgins, D. C.; Bao, Z.; Jaramillo, T. F. Understanding the Origin of Highly Selective CO_2 Electroreduction to CO on Ni,N-doped Carbon Catalysts. *Angew. Chem., Int. Ed.* **2020**, *59*, 4043−4050.
(48) Huan, T. N.; Ranjbar, N.; Rousse, G.; Sougrati, M.; Zitolo, A.; Mougel, V.; Jaouen, F.; Fontecave, M. Electrochemical reduction of CO_2 catalyzed by Fe-NC materials: A structure−selectivity study. *ACS Catal.* **2017**, *7*, 1520−1525.
(49) Masel, R. I.; Liu, Z.; Yang, H.; Kaczur, J. J.; Carrillo, D.; Ren, S.; Salvatore, D.; Berlinguette, C. P. An industrial perspective on catalysts for low-temperature CO_2 electrolysis. *Nat. Nanotechnol.* **2021**, 118−128.
(50) Gu, Z.; Shen, H.; Chen, Z.; Yang, Y.; Yang, C.; Ji, Y.; Wang, Y.; Zhu, C.; Liu, J.; Li, J.; Sham, T.-K.; Xu, X.; Zheng, G. Efficient Electrocatalytic CO_2 Reduction to C_{2+} Alcohols at Defect-Site-Rich Cu Surface. *Joule* **2021**, *5*, 429−440.
(51) Chen, X.; Chen, J.; Alghoraibi, N. M.; Henckel, D. A.; Zhang, R.; Nwabara, U. O.; Madsen, K. E.; Kenis, P. J. A.; Zimmerman, S. C.; Gewirth, A. A. Electrochemical CO_2-to-ethylene conversion on polyamine-incorporated Cu electrodes. *Nat. Catal.* **2021**, *4*, 20−27.
(52) Li, J.; Li, P.; Li, J.; Tian, Z.; Yu, F. Highly-Dispersed Ni-NiO Nanoparticles Anchored on an SiO_2 Support for an Enhanced CO Methanation Performance. *Catalysts* **2019**, *9*, 506.
(53) Fina, F.; Callear, S. K.; Carins, G. M.; Irvine, J. T. S. Structural Investigation of Graphitic Carbon Nitride via XRD and Neutron Diffraction. *Chem. Mater.* **2015**, *27*, 2612−2618.
(54) Pan, F.; Li, B.; Deng, W.; Du, Z.; Gang, Y.; Wang, G.; Li, Y. Promoting electrocatalytic CO_2 reduction on nitrogen-doped carbon with sulfur addition. *Appl. Catal., B* **2019**, *252*, 240−249.
(55) Li, J.-C.; Hou, P.-X.; Zhao, S.-Y.; Liu, C.; Tang, D.-M.; Cheng, M.; Zhang, F.; Cheng, H.-M. A 3D bi-functional porous N-doped carbon microtube sponge electrocatalyst for oxygen reduction and oxygen evolution reactions. *Energy Environ. Sci.* **2016**, *9*, 3079−3084.
(56) De Fazio, D.; Goykhman, I.; Yoon, D.; Bruna, M.; Eiden, A.; Milana, S.; Sassi, U.; Barbone, M.; Dumcenco, D.; Marinov, K.; Kis, A.; Ferrari, A. C. High Responsivity, Large-Area Graphene/MoS_2 Flexible Photodetectors. *ACS Nano* **2016**, *10*, 8252−8262.
(57) Ferrari, A. C.; Basko, D. M. Raman spectroscopy as a versatile tool for studying the properties of graphene. *Nat. Nanotechnol.* **2013**, *8*, 235−246.
(58) Li, M.; Carter, R.; Cohn, A. P.; Pint, C. L. Interconnected foams of helical carbon nanofibers grown with ultrahigh yield for high capacity sodium ion battery anodes. *Carbon* **2016**, *107*, 109−115.
(59) Wang, Y.; Han, P.; Lv, X.; Zhang, L.; Zheng, G. Defect and Interface Engineering for Aqueous Electrocatalytic CO_2 Reduction. *Joule* **2018**, *2*, 2551−2582.
(60) Pan, F.; Li, B.; Sarnello, E.; Fei, Y.; Feng, X.; Gang, Y.; Xiang, X.; Fang, L.; Li, T.; Hu, Y. H.; Wang, G.; Li, Y. Pore-Edge Tailoring of Single-Atom Iron-Nitrogen Sites on Graphene for Enhanced CO_2 Reduction. *ACS Catal.* **2020**, *10*, 10803−10811.
(61) Wu, Q.; Gao, J.; Feng, J.; Liu, Q.; Zhou, Y.; Zhang, S.; Nie, M.; Liu, Y.; Zhao, J.; Liu, F.; Zhong, J.; Kang, Z. A CO_2 adsorption dominated carbon defect-based electrocatalyst for efficient carbon dioxide reduction. *J. Mater. Chem. A* **2020**, *8*, 1205−1211.
(62) Li, C.; Yang, X.; Yang, B.; Yan, Y.; Qian, Y. Synthesis and characterization of nitrogen-rich graphitic carbon nitride. *Mater. Chem. Phys.* **2007**, *103*, 427−432.
(63) Gang, Y.; Pan, F.; Fei, Y.; Du, Z.; Hu, Y. H.; Li, Y. Highly Efficient Nickel, Iron and Nitrogen Co-Doped Carbon Catalysts Derived from Industrial Waste Petroleum Coke for Electrochemical CO_2 Reduction. *ACS Sustainable Chem. Eng.* **2020**, *8*, 8840−8847.
(64) Zhang, N.; Zhou, T.; Chen, M.; Feng, H.; Yuan, R.; Zhong, C.'a.; Yan, W.; Tian, Y.; Wu, X.; Chu, W.; Wu, C.; Xie, Y. High-purity pyrrole-type FeN_4 sites as a superior oxygen reduction electrocatalyst. *Energy Environ. Sci.* **2020**, *13*, 111−118.
(65) Pan, F.; Liang, A.; Duan, Y.; Liu, Q.; Zhang, J.; Li, Y. Self-growth-templating synthesis of 3D N,P, Co-doped mesoporous

https://doi.org/10.1021/acscatal.1c01864
ACS Catal. 2021, 11, 10333−10344

carbon frameworks for efficient bifunctional oxygen and carbon dioxide electroreduction. *J. Mater. Chem. A* **2017**, *5*, 13104−13111.
(66) Liu, J.; Zhang, T.; Wang, Z.; Dawson, G.; Chen, W. Simple pyrolysis of urea into graphitic carbon nitride with recyclable adsorption and photocatalytic activity. *J. Mater. Chem.* **2011**, *21*, 14398−14401.
(67) Briggs, D.; Briggs, D. J. *Surface analysis of polymers by XPS and static SIMS*; Cambridge University Press: 2009.
(68) Russell, A. E.; Rose, A. X-ray absorption spectroscopy of low temperature fuel cell catalysts. *Chem. Rev.* **2004**, *104*, 4613−4636.
(69) Fan, Q.; Hou, P.; Choi, C.; Wu, T.-S.; Hong, S.; Li, F.; Soo, Y.-L.; Kang, P.; Jung, Y.; Sun, Z. Activation of Ni Particles into Single Ni-N Atoms for Efficient Electrochemical Reduction of CO_2. *Adv. Energy Mater.* **2020**, *10*, 1903068.
(70) Wu, G.; More, K. L.; Johnston, C. M.; Zelenay, P. High-performance electrocatalysts for oxygen reduction derived from polyaniline, iron, and cobalt. *Science* **2011**, *332*, 443−447.
(71) Li, H.; Liu, X.; Chen, S.; Yang, D.; Zhang, Q.; Song, L.; Xiao, H.; Zhang, Q.; Gu, L.; Wang, X. Edge-Exposed Molybdenum Disulfide with N-Doped Carbon Hybridization: A Hierarchical Hollow Electrocatalyst for Carbon Dioxide Reduction. *Adv. Energy Mater.* **2019**, *9*, 1900072.
(72) Hu, X.-M.; Hval, H. H.; Bjerglund, E. T.; Dalgaard, K. J.; Madsen, M. R.; Pohl, M.-M.; Welter, E.; Lamagni, P.; Buhl, K. B.; Bremholm, M.; Beller, M.; Pedersen, S. U.; Skrydstrup, T.; Daasbjerg, K. Selective CO_2 reduction to CO in water using earth-abundant metal and nitrogen-doped carbon electrocatalysts. *ACS Catal.* **2018**, *8*, 6255−6264.
(73) Zheng, Y.; Jiao, Y.; Zhu, Y.; Cai, Q.; Vasileff, A.; Li, L. H.; Han, Y.; Chen, Y.; Qiao, S.-Z. Molecule-Level g-C_3N_4 Coordinated Transition Metals as a New Class of Electrocatalysts for Oxygen Electrode Reactions. *J. Am. Chem. Soc.* **2017**, *139*, 3336−3339.
(74) Feng, J.; Gao, H.; Zheng, L.; Chen, Z.; Zeng, S.; Jiang, C.; Dong, H.; Liu, L.; Zhang, S.; Zhang, X. A Mn-N_3 single-atom catalyst embedded in graphitic carbon nitride for efficient CO_2 electroreduction. *Nat. Commun.* **2020**, *11*, 4341.
(75) Li, X.; Zhang, J.; Shen, L.; Ma, Y.; Lei, W.; Cui, Q.; Zou, G. Preparation and characterization of graphitic carbon nitride through pyrolysis of melamine. *Appl. Phys. A* **2009**, *94*, 387−392.
(76) May, H. Pyrolysis of melamine. *J. Appl. Chem.* **1959**, *9*, 340−344.
(77) Jeng, E.; Jiao, F. Investigation of CO_2 single-pass conversion in a flow electrolyzer. *React. Chem. Eng.* **2020**, *5*, 1768−1775.
(78) Larrazábal, G. O.; Ma, M.; Seger, B. A Comprehensive Approach to Investigate CO_2 Reduction Electrocatalysts at High Current Densities. *Acc. Mater. Res.* **2021**, *2*, 220−229.
(79) Zhang, X.; Li, J.; Li, Y.-Y.; Jung, Y.; Kuang, Y.; Zhu, G.; Liang, Y.; Dai, H. Selective and High Current CO_2 Electro-Reduction to Multicarbon Products in Near-Neutral KCl Electrolytes. *J. Am. Chem. Soc.* **2021**, *143*, 3245−3255.
(80) Xu, Y.; Edwards, J. P.; Liu, S.; Miao, R. K.; Huang, J. E.; Gabardo, C. M.; O'Brien, C. P.; Li, J.; Sargent, E. H.; Sinton, D. Self-Cleaning CO_2 Reduction Systems: Unsteady Electrochemical Forcing Enables Stability. *ACS Energy Lett.* **2021**, *6*, 809−815.

https://doi.org/10.1021/acscatal.1c01864
ACS Catal. 2021, 11, 10333−10344